APEM journal
Advances in Production Engineering & Management
Volume 14 | Number 4 | December 2019 | pp 407–420
https://doi.org/10.14743/apem2019.4.337
ISSN 1854-6250
Journal home: apem-journal.org
Original scientific paper

Femtosecond laser helical drilling of nickel-base single-crystal super-alloy: Effect of machining parameters on geometrical characteristics of micro-holes

Yin, C.P.[a], **Wu, Z.P.**[a], **Dong, Y.W.**[a,b,*], **You, Y.C.**[a], **Liao, T.**[a]

[a]School of Aerospace Engineering, Xiamen University, Xiamen, P.R. China
[b]Shenzhen Research Institute, Xiamen University, Shenzhen, P.R. China

ABSTRACT

Laser micro-hole processing has been widely used in industry. Many laser processing parameters can affect the processing results. The relationship between the geometrical shapes of micro-holes and the laser processing parameters has not been determined accurately. In this paper, experiments on the femtosecond laser drilling of the nickel-base single-crystal super-alloy (DD6) materials were conducted to determine the relationship between the parameters, such as the laser single-pulse energy, rotation rate, and downward focus rate, and the geometrical characteristics of the micro-holes, such as the diameter, and roundness. A group of orthogonal experiments were conducted to determine the effects of the comprehensive influencing factors on the geometrical characteristics of the micro-holes. After the experiments were conducted and analysed, the experimental results were modelled by a backpropagation neural network, and the mapping relationship between the laser parameters and the geometrical morphologies of the micro-holes was constructed. The model established by the backpropagation neural network could obtain accurate prediction results, and the predictions of the diameters of the micro-holes were better than those of the roundness.

ARTICLE INFO

Keywords:
Femtosecond laser;
Micro-hole machining;
Helical drilling;
Nickel-base single-crystal super-alloy (DD6);
Orthogonal experiment;
Artificial neural networks (ANN)

**Corresponding author:*
yiweidong@xmu.edu.cn
(Dong, Y.W.)

Article history:
Received 26 November 2019
Revised 10 December 2019
Accepted 11 December 2019

1. Introduction

Laser micromachining has many applications in material processing, and it has received considerable attention because it can be used in nearly all of the manufacturing sectors [1], such as in the fields of aerospace, the electronics industry [2], biomedical engineering [3], measurement instruments, and the automotive industry [4]. With the rapid development of all these manufacturing sectors, the accuracy requirements of the laser technology have become stricter. The short pulse or even ultarshort pulse laser (pulse duration < 10 ps) has become a reliable technology for manufacturing and production [5] and considered to be a better choice for micro-hole drilling due to its high efficiency, low loss, noncontact procession without any special fixtures for the workpiece [6].

Laser drilling is one of the earliest laser machining technologies used in industry. Since the end of the 1990s, femtosecond lasers have been powerful tools in solid materials machining [7]. Compared with traditional long pulse lasers, femtosecond lasers have advantages in ultra-fine processing, from the submicron scale to the nanoscale, due to their extremely high peak power and multiphoton process with the materials. This advantage lies in limiting the range of energy

in a small interspace in the center of focus, and not the whole area of irradiation by adjusting the incident energy. Furthermore, another advantage is the versatility in the types of materials that can be processed by femtosecond laser micromachining, such as metals, glasses, polymers, plastics, and semiconductor [8]. The multiphoton absorption and ionization threshold only hinges upon the atomic properties of the materials, not the concentration of free electrons. Theoretically speaking, the range of the heat-affected zone in femtosecond laser micromachining processing is negligible [9], and thus, non-hot melt processing with high precision is available. Due to its ultrashort pulse duration acting on the materials in short periods of time with high power densities, the energy absorption can be controlled only in the machining region and cause materials to enter the plasma state while materials outside the machining region remains cold without heat diffusion.

The laser drilling process is a preferred method due to its unique properties of no tool wear, flexibility, and high rates [10]. Laser processing parameters have important influences on quality, efficiency, and cost. The main research parameters include the wavelength, pules width, spot radius, pules energy, repeat frequency, and rotation rate [11, 12], which directly affects the dimensional and shape accuracy of the processed micro-holes. Furthermore, there are four common strategies in laser drilling: single pulse percussion drilling, multiple pulse percussion drilling, rotary trepanning and helical drilling [13] as shown in Fig. 1 [14]. In percussion drilling, laser pulses shaped as voxels of a particular size are focused on a desired location for the desired time to ablate materials with the same geometric dimensions as those of the voxels. For trepanning and helical drilling, the laser pulse moves in a circular route to the required diameter of the presupposed micro-hole [15].

Although the application of femtosecond laser in drilling has attracted considerable attention in academia and industry, there are few accurate quantitative models that can describe the relationship between the laser parameters and geometrical shape of the micro-holes. In practice, the selection of parameters always depends on experiences of previous experiments, and the geometrical parameters of the micro-holes are difficult to forecast before machining. Therefore, it is vital to establish certain mapping relations between the processing parameters and geometric features.

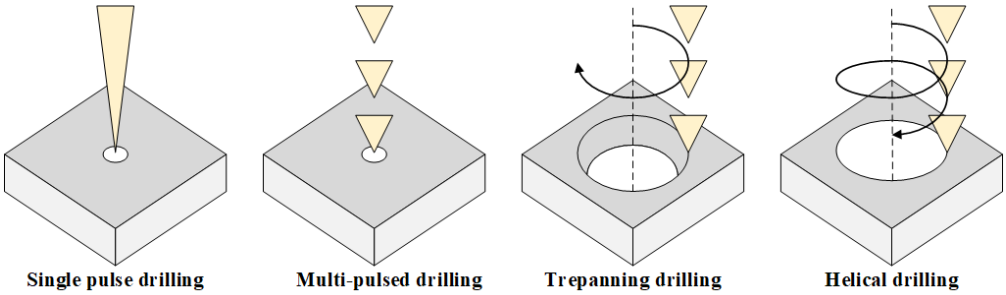

Fig. 1 Four micro-hole drilling strategies: From the left to right are single pulse percussion drilling, multiple pulse percussion drilling, rotary trepanning, and helical drilling

2. Materials and methods

2.1 Experimental equipment and methods

In the first experiment, lasers with different single-pulse energies, rotation rates, and downward focus rates were used to perform helical drilling. In addition, a group of $L_{25}(5^4)$ orthogonal experiments are processed to determine the comprehensive influences of the single-pulse energy, rotation rate, and downward focus rate on the geometrical parameters of the micro-holes. The machined material was a nickel-base single crystal super-alloy (DD6) with a thickness of 1 mm. The basic parameters of the laser system are listed in Table 1. A KH7040A-1 5-axis numerical control machine with PHAROS high power and energy femtosecond lasers was used, as shown in Fig. 2. The schematic diagram of the femtosecond laser machining system is shown in Fig. 3. Although the polarization state of the light mainly affects the roundness and the surface accuracy of

the micro-holes, there was no significant difference between polarized light in the quality of the micro-holes from the helical drilling [16]. Therefore, the influence of the laser polarization state factor was not considered. In the experiment, the quarter-wave plate (B) was used to convert the laser light into circularly polarized light and then focused on the surface of the processed materials. A four-optical-wedge beam rotation apparatus (E) is used to deflect the laser beam to achieve a planar helical motion. The rotary cutting module was composed of the focusing lens (F), and the laser outlet nozzle (G) could move along the material surface perpendicularly. By controlling the vertical adjustment device (H), the downward focus rate could be controlled, and combined with the planar helical movement, helical drilling could be achieved. The projection of the machining path is shown in Fig. 4, with a 0.5 mm radius of the outermost ring. The features of the micro-holes were observed and measured using SUPRA55 field emission gun scanning electron microscope (SEM). After machining, the specimens were soaked in ethanol solution and cleaned ultrasonically to remove the liquid melt on the surfaces of the specimens before the SEM measurements.

Table 1 Parameters of laser machining system

Parameter	Unit	Range
Average power	W	0-15
Pulse width	fs	250
Repetition rate	kHz	60-600
Wavelength	nm	1064
Focal distance	mm	150
Air blowing pressure	MPa	0-0.5
Rotation rate	r/min	600-2400
Spot radius	μm	15-25

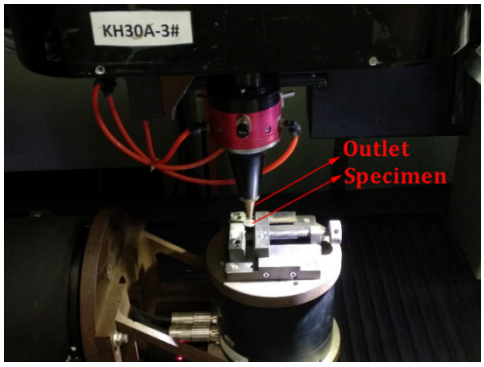

Fig. 2 Photo of laser device and specimen

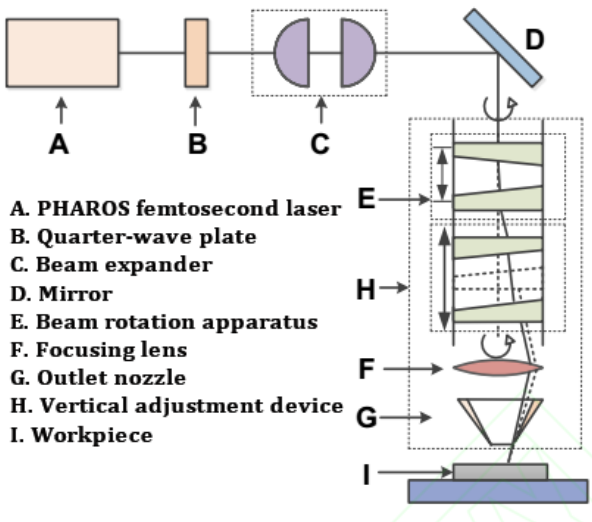

Fig. 3 The schematic diagram of the femtosecond laser machining system

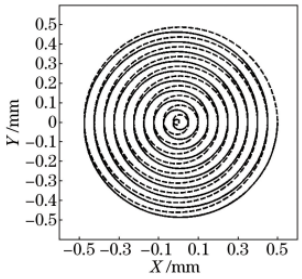

Fig. 4 The projection of the laser helical scanning path

2.2 Single factor experiments, helical micro-hole machining, trepanning machining

The first experiment was to determine the influence of the single-pulse energy on the features of micro-holes. The parameters that describe the features include the diameters, the roundness of entrance and exit, and the taper of each hole. The roundness of a micro-hole Δr can be calculated by the difference of diameters of the outer contour C_1 and inner contour C_2 [17].

$$\Delta r = C_1 - C_2 \tag{1}$$

The outer contour is the minimum circumscribed circle of the hole, while the inner contour means the maximum inscribed circle of the hole. A smaller Δr means a more circular and less rough hole.

The taper can be calculated by Eq. 2.

$$Taper = 2 \times tan^{-1} \frac{R_1 - R_2}{2000} \tag{2}$$

where R_1 and R_2 denote the entrance and exit diameters, respectively.

The focus of the laser was set on the platform of the specimen with a repetition rate of 100 kHz, rotation rate of 2400 r/min, and maximum processing time of 200 s. The single-pulse energy was set from 80 to 130 μJ at intervals of 10 μJ.

The second experiment examined the relationship between the rotation rate and the features of the micro-holes. Similar to the first experiment, the focus was set on the platform of the specimen with a repetition rate of 100 kHz, single pulse energy of 100 μJ, and maximum processing time of 200 s. The rotation rate was set from 600 to 2400 r/min at intervals of 300 r/min.

The third experiment aims to explore the effect of the focus downward rate on helical laser micro-holes drilling. The downward focus rate was set from 0 to 0.03 mm/s at intervals of 0.005 mm/s. The repetition rate was set to 100 kHz, the single-pulse energy was set to 100 μJ, and the rotation rate was set to 2400 r/min. The processing time was 100 s.

For all of the experiments above, blowing pressure was set to 0.5 MPa. For each set of data, three drilling processes were conducted and the average was obtained.

2.3 Orthogonal experimental design (OED)

To investigate the effect and significance of the single-pulse energy, the rotation rate and the downward focus rate on the geometric characteristics, such as the diameters and roundness of the entrance and exit of the micro-hole, the backpropagation (BP) neural network (BPNN) was used to obtain the mapping relationship between the geometric characteristics of the micro-holes and these parameters. $L_{25}(5^4)$ orthogonal experiments with three processing parameters were designed, as it can get influence relationship between experimental variables through a small amount of experiments. In the OED, the occurrence frequencies of the levels in each column were the same, and the number of occurrences of an ordinal number pair consisting of all of the data in any two columns was the same. This ensured a uniform dispersion of the experimental conditions and eliminated the interference from other factors [18]. As shown in Table 2, a blank column was designated for the error evaluation, and five levels were set for each factor. The laser repetition rate was set to 100 kHz and the blowing pressure was 0.5 MPa. The processing time was 200 s for each micro-hole.

Table 2 Factors and levels of orthogonal experiments

Level \ Factor	A Single pulse energy, μJ	B Rotation rate, (r·min^{-1})	C Focus downward rate, (mm·s^{-1})	Blank
1	60	1600	0.005	
2	70	1800	0.01	
3	80	2000	0.015	
4	90	2200	0.02	
5	100	2400	0.025	

3. Results and discussion

3.1 Effect of single pulse energy

Fig. 5 shows the variation of the diameters and roundness of the micro-holes with the single-pulse energy. This indicates that, for the exit diameter, there was a leap between 100 μJ to 110 μJ in the single-pulse energy from 543.29 μm to 951.97 μm. When the single-pulse energy is no more than 100 μJ, the shapes of the exits of the micro-holes deviate significantly from a circle, which means that for a better drilling result, a threshold of single-pulse energy is needed when the other related processing parameters are fixed. Fig. 6 shows the SEM photos of the hole exit with single pulse energy of 80 μJ and 110 μJ, the disparity of roundness is obvious. In fact, a laser with a higher single-pulse energy can produce a high metal vapor pressure that can carry away more material in a molten or liquid state [19]. Furthermore, the laser energy followed a Gaussian distribution, which caused the diameter of the focus on the processed material to increase with increasing pulse energy. During ablation, heat transfer occurred. Although the heat transfer was weak at any instant, its cumulative effect could not be neglected. The scanning path of helical drilling causes the laser to not only process at a certain point, which greatly reduces the heat accumulation and increases the heat release [20]. As the single-pulse energy increased, the entrance and exit diameters increased to maximum values and stayed in the range of about 1050 μm and 958 μm, and the taper decreased from 0.52 and remained at approximately 0.1. The roundness of the entrance and exit exhibited similar patterns, with diameters of approximately 22 μm and 68 μm.

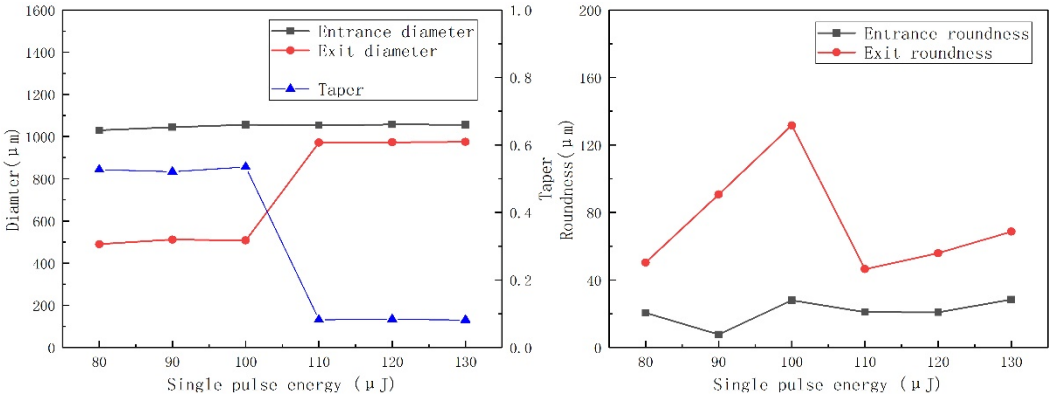

Fig. 5 Geometric characteristics change to single pulse energy

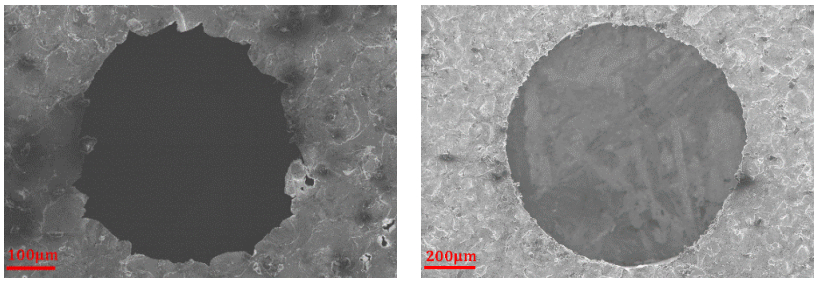

Fig. 6 Photos of the exit hole with single pulse energy of 80 μJ and 110 μJ

3.2 Effect of rotation rate

Fig. 7 shows the variation of the diameters, roundness and tapers of the micro-holes with the rotation rate. This indicates that the entrance diameter increased from the top at 1066.68 μm, then decreased and remained steady around 1045 μm as the rotation rate goes up. The exit diameter remained in the range between 937 μm to 952 μm. The entrance roundness decreased overall, but the exit roundness increased generally. The rotation rate significantly influenced the exit roundness, because as the rotation rate increased, the number of pulses during a single scanning cycle was reduced. Therefore, the effect of the rotation rate on the processing was essentially due to changes in the number of pulses. The reduction in the number of pulses during one processing cycle resulted in layer-by-layer processing to the bottom, and the corresponding reduction in the amount of erosion caused the exit roundness to deteriorate. The taper remained at approximately 0.1. Compared with other parameters, there was less influence of the rotation rate on the entrance and exit diameters of the micro-holes because the variation of the rotation rate did not affect the number and power of pulse acting on the material. Furthermore, the thermal incubation effect was not evident because the laser spot did not focus on only one area during helical drilling [21].

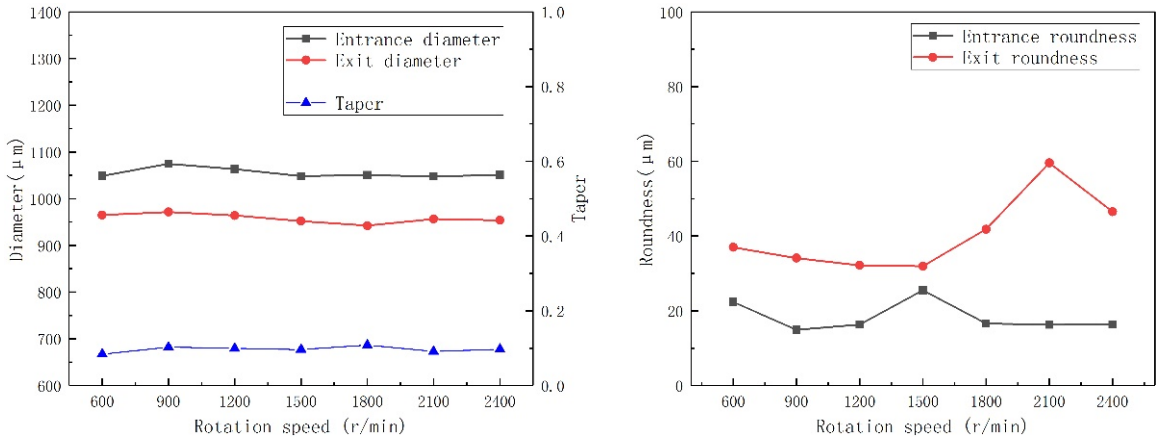

Fig. 7 Geometric characteristics change to rotation rate

3.3 Effect of focus downward rate

Fig. 8 shows the variation of the parameters of the micro-holes with the downward focus rate. When the downward focus rate increased, the entrance and exit diameters exhibited the opposite trend, and thus, a sharp drop in the taper occurred. The entrance roundness remained between 20 μm and 30 μm, whereas the exit roundness fluctuated significantly. The downward focus rate was strongly connected to the defocusing amount, which is an important factor influencing the features of the micro-holes [22]. Most of the energy of the laser beam distributed over a certain range of focal depths. The focal plane was where the diameter of the beam waist was at a minimum. Defocusing means the focal plane is not coincident, the deviation distance between which is called the defocusing amount [23]. Fig. 9 shows from left to right illustrations of negative, zero, and positive defocusing. As the focal point moved downward, the negative defocusing amount causes a transition of the phase to occur only by heat transfer on the walls of the micro-holes. A lower ratio of gaseous to molten or liquid states causes the residues to remain bounded at the edges of holes, which enlarged heat-affected zone and decreased the area of the effective heat transfer region. As the focus moved downward, only part of the material on the surface could be melted, whereas the energy of the laser beam concentrated on the focal position moved closer to the back face of the material. Thus, the entrance diameter decreased and the exit diameter increased, causing the taper decreased as the downward focus rate increased. Fig. 10 is the photos of the entrance hole with focus downward rate of 0 and 0.03 mm/s. The difference of the taper is obvious. Influenced by residues, the non-uniform heating contributed to the great fluctuation of the exit roundness. In addition, the appearance of the cone and the change of the taper

were related to the incident angle of the laser. According to the Fresnel effect [24], when the incident angle of a laser increases, the absorption rate of materials will decrease. During processing, changing the distribution of the laser radiation intensity led to the formation of a cone. When the laser irradiated the micro-holes, the walls could not absorb all the energy, and ablation rate decreased gradually [20]. When the energy density absorbed by the material was lower than the ablation threshold, the ablation process ended.

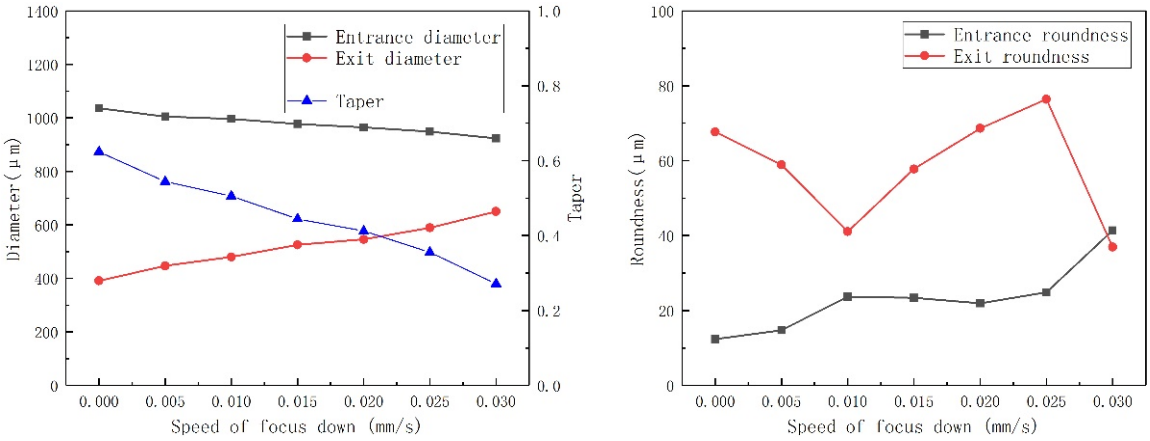

Fig. 8 Geometric characteristics change to focus downward rate

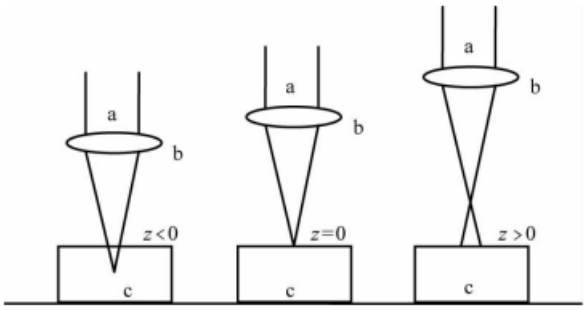

Fig. 9 Schematic diagram of the defocusing amount. 'a' is the laser beam; 'b' is the lens and 'c' is the processed material.

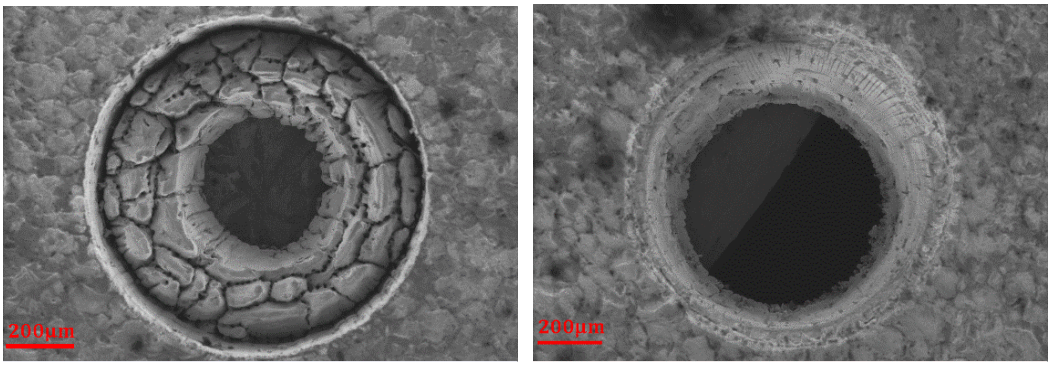

Fig. 10 Photos of entrance hole with focus downward rate of 0 and 0.03 mm/s

3.4 Orthogonal experimental design result and analysis

The orthogonal experiment results are shown in Table 3. For training and testing the BPNN, another group of experiments are designed and processed (Table 4).

Range and variance analyses [25] are common methods for investigating the influence of each factor on the experiment results. In range analysis, the order of influence of the factors on the results can be seen by comparing the ranges of each factor. There are two parameters in the range analysis, T and R. T is defined as the sum of all of the results in the experiments. T_i denotes the sum of the results of level i in a column. R is defined as the range between the maximum and minimum of T_i for each factor.

$$R = max(T_i) - min(T_i) \tag{3}$$

Table 3 Orthogonal experiment result

Test number	A Single pulse energy, μJ	B Rotation rate, (r·min^{-1})	C Focus downward rate, (mm·s^{-1})		Entrance diameter, μm	Exit diameter, μm	Entrance roundness, μm	Exit roundness, μm
1	60	1600	0.005	1	1032.06	512.46	48.59	56.50
2	60	1800	0.015	3	922.87	661.28	47.30	41.22
3	60	2000	0.025	5	909.87	511.11	36.94	48.41
4	60	2200	0.01	2	1004.80	525.93	33.07	31.10
5	60	2400	0.02	4	911.47	577.78	36.31	52.07
6	70	1600	0.025	2	919.27	604.71	37.91	33.52
7	70	1800	0.01	4	995.20	592.59	28.64	51.60
8	70	2000	0.02	1	937.60	644.44	28.09	41.97
9	70	2200	0.005	3	1036.80	550.61	36.98	61.72
10	70	2400	0.015	5	990.47	723.46	39.24	44.74
11	80	1600	0.02	3	947.20	701.23	32.99	48.25
12	80	1800	0.005	5	1034.00	952.78	36.00	43.44
13	80	2000	0.015	2	988.90	806.98	32.22	50.44
14	80	2200	0.025	4	935.80	617.28	42.48	42.86
15	80	2400	0.01	1	1008.00	850.74	42.39	23.14
16	90	1600	0.015	4	976.00	814.91	48.30	50.25
17	90	1800	0.025	1	921.60	650.94	39.90	25.99
18	90	2000	0.01	3	1017.60	872.73	34.40	29.09
19	90	2200	0.02	5	957.60	708.07	38.78	29.61
20	90	2400	0.005	2	1038.18	960.74	37.26	28.06
21	100	1600	0.01	5	1022.72	915.56	23.60	22.40
22	100	1800	0.02	2	944.40	763.40	31.82	30.98
23	100	2000	0.005	4	1040.72	960.27	32.56	25.74
24	100	2200	0.015	1	989.60	836.60	31.04	42.75
25	100	2400	0.025	3	940.80	718.01	36.08	24.94

Table 4 Supplemental experiments for BPNN modelling

Test number	A Single pulse energy, μJ	B Rotation rate, (r·min^{-1})	C Focus downward rate, (mm·s^{-1})	Entrance diameter, μm	Exit diameter, μm	Entrance roundness, μm	Exit roundness, μm
B1	60	1600	0.015	915.2	658.59	37.18	52.87
B2	60	1800	0.025	905.12	505.35	41.09	68.56
B3	70	2200	0.02	921.6	654.86	40.71	51.82
B4	80	2400	0.005	1039.98	949.25	38.45	56.19
B5	80	1600	0.015	983.2	777.78	30.05	49.13
B6	90	2000	0.025	918.9	684.44	39.64	27.54
B7	90	1800	0.01	1008.4	884.44	34.48	29.28
B8	100	2200	0.02	942.4	874.93	32.17	38.37
B9	100	2400	0.005	1036.8	969.33	38.88	28.34

The greater the value of *R* of the factor is, the greater the influence of the factor is on the result.

The range analysis can be used to determine the impact order of the factors intuitively, but the experimental error cannot be estimated. Moreover, the impact magnitudes of the factors cannot be indicated, especially for the OED with more than three levels. Considering the limitation of range analysis, variance analysis is necessary to determine the impact degrees or magnitudes of the factors on the results. The most important parameters in the variance analysis are the sum of squared deviations for the total, for each column, and error.

The total sum of squared deviation (SST) and the total freedom (f_T) are defined as follows:

$$SST = \sum_{i=1}^{n} (x_i - \bar{x})^2 \tag{4}$$

$$f_T = n - 1 \tag{5}$$

The sum of squared deviations for each factor (SS_j) and the freedom for each (f_j) are defined as follows:

$$SS_j = \frac{1}{r}\sum_{i=1}^{m} {T_i}^2 - \frac{T^2}{n} \tag{6}$$

$$f_j = m - 1 \ (j = 1,2, \dots, k-1) \tag{7}$$

The sum of squared deviations for the experimental error (SSE) and its freedom (f_e) are defined as follows:

$$\mathrm{SSE} = \mathrm{SST} - \sum_{j=1}^{k} SS_j \tag{8}$$

$$f_e = f_T - \sum_{j=1}^{k} f_j \tag{9}$$

The variances of each factor (MS_j) and the one of experimental error (MSE) can be calculated by as follows:

$$MS_j = \frac{SS_j}{f_j} \tag{10}$$

$$MSE = \frac{SSE}{f_e} \tag{11}$$

where the *F* value is used to illustrate the magnitudes of the effects on the factors. This reflects the ratio of the sum of squared deviations of each factor to that of the experimental error. Thus, the *F* value of each factor is as follows:

$$F_j = \frac{MS_j}{MSE} \tag{12}$$

In Eqs. 4 to 12, $n = 25$, $m = 5$, $k = 4$, and $r = n/m = 5$ for $L_{25}(5^4)$ OED.

In the *F*-distribution table, comparing F_j with the value of $F_\alpha(f_T, f_e)$ can determine whether the factor effect on the results is prominent or not, which is called the *F*-test. If F_j is larger than F_α, the factor effect on the results is prominent and vice versa. Usually, α = 0.05 is the demarcation of prominence, and α = 0.01 is the demarcation of high prominence [26]. In addition, if the variance of a factor is less than double the variance of the experimental error ($MS_j < 2\ MSE$), this factor can be seen as an error and its squared deviation and freedom will be added to those of the error. In the result tables, the factors meeting this criterion are marked with an asterisk '*'.

The results of the range and variance analysis are shown in Table 5-12. All of the three factors have significant influences on the hole diameters, while the downward focus rate and the single-pulse energy are the most important factors affecting the entrance and exit diameter results, respectively. For the roundness, the rotation rate was the weakest factor, and the single-pulse energy was the main influencing factor. In the range of experimental data, there was a positive

correlation between the diameters and the single-pulse energy and a negative correlation between diameters and downward focus rate. The effect of rotation rate on diameters is fluctuant. On the whole, the increase in the single-pulse energy was helpful for reducing roundness, especially for the hole exit. The entrance roundness was lower than the exit roundness in general. With a greater pulse energy, more photon energy can be absorbed by the materials. The stronger capability of laser to remove materials makes micro-holes more circular [27]. Fig. 11 represents the exit of the hole processed with single pulse energy at 80 μJ, Rotation rate at 2400 r/min and focus downward rate at 0.01 mm/s. In comparison with the exit hole shown in Fig. 6, the focus moving down is beneficial to the exit hole for its roundness. Defocusing can improve heat transfer through the interior from entrance to exit and material at the back-side can receive the energy from laser more evenly and sufficiently.

Table 5 Range analysis for entrance diameters

	A	B	C	Blank
T1	4781.07	4897.25	5181.76	4888.86
T2	4879.34	4818.07	5048.32	4895.55
T3	4913.90	4894.69	4867.84	4865.27
T4	4910.98	4924.60	4698.27	4859.19
T5	4938.24	4888.92	4627.34	4914.66
R	157.17	106.53	554.42	55.37
Order	CAB			

Table 6 Variation analysis for entrance diameters

Source of variation	Sum of squares	Freedom	Variance	*F*-value	Critical value of *F*-test (F_α)	Significance
A	3035.54	4	758.89	22.09	$F_{0.05}$ = 3.2592	High
B	1261.34	4	315.33	9.18	$F_{0.01}$ = 5.412	High
C	43258.14	4	10814.54	314.85		High
Blank*	412.18	4	103.05	3.00		
Other errors	412.18	12	34.35			
Total	47967.21	24				

Table 7 Range analysis for exit diameters

	A	B	C	Blank
T1	2788.56	3548.87	3936.86	3495.18
T2	3115.81	3620.99	3757.55	3551.76
T3	3929.01	3795.53	3843.23	3503.86
T4	4007.39	3238.49	3394.92	3562.83
T5	4193.84	3830.73	3102.05	3810.98
R	1405.28	592.24	834.81	315.8
Order	ACB			

Table 8 Variance analysis for exit diameters

Source of variation	Sum of squares	Freedom	Variance	*F*-value	Critical value of *F*-test (F_α)	Significance
A	303899.08	4	75974.78	65.40	$F_{0.05}$ = 3.2592	High
B	44994.62	4	11248.65	9.69	$F_{0.01}$ = 5.412	High
C	97445.99	4	24361.50	20.97		High
Blank*	13939.81	4	3484.95	3.00		
Other errors	13939.81	12	1161.65			
Total	460279.49	24				

Table 9 Range analysis for entrance roundness

	A	B	C	Blank
T1	202.21	191.39	191.39	190.01
T2	170.86	183.66	162.10	172.28
T3	186.08	164.21	198.10	187.75
T4	198.64	182.35	167.99	188.29
T5	155.10	191.28	193.31	174.56
R	47.11	27.18	36.00	17.73
Order	ACB			

Table 10 Variation analysis for entrance roundness

Source of variation	Sum of squares	Freedom	Variance	*F*-value	Critical value of *F*-test (F_α)	Significance
A	309.604	4	77.40	7.97	$F_{0.05}$ = 3.0069	High
B*	98.40	4	24.60	2.53	$F_{0.01}$ = 4.7726	
C	213.18	4	53.30	5.49		High
Blank*	56.99	4	14.28	1.49		
Other errors	155.39	16	9.71			
Total	678.17	24				

Table 11 Range analysis for exit roundness

	A	B	C	Blank
T1	229.30	210.92	215.46	190.35
T2	233.55	193.23	157.33	174.10
T3	208.13	195.65	229.40	205.22
T4	163.00	208.04	202.88	222.52
T5	146.81	172.95	175.72	188.60
R	86.74	37.97	48.42	
Order	ACB			

Table 12 Variation analysis for exit roundness

Source of variation	Sum of squares	Freedom	Variance	*F*-value	Critical value of *F*-test (F_α)	Significance
A	1234.91	4	308.73	10.92	$F_{0.05}$ = 3.0069	High
B*	181.31	4	45.33	1.60	$F_{0.01}$ = 4.7726	
C	689.62	4	172.41	6.10		High
Blank*	270.90	4	67.72	2.40		
Other errors	452.21	16	28.26			
Total	2376.74	24				

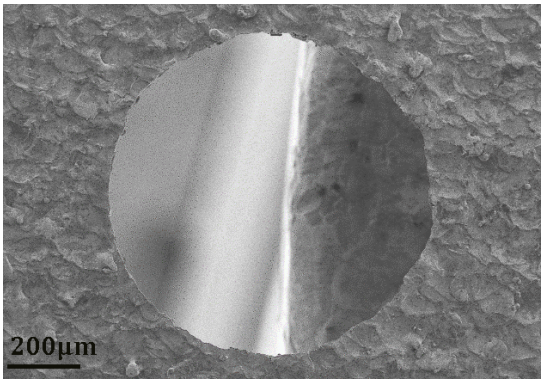

Fig. 11 Photo of the exit of the hole processed with single pulse energy of 80 μJ, rotation rate of 2400 r/min, and focus downward rate of 0.01 mm/s

3.5 Prediction of micro-hole geometry characteristics with back propagation artificial neural network (ANN), modelling with artificial neural network, testing of the model

Containing functions of self-learning and self-training, artificial neural networks (ANNs) are suitable for finding relationships between data inputs and outputs, especially for nonlinear data. In general, a neural network can be seen as a mapping relationship between input and output variables [28]. Similar to a biological brain, a neuron is the basic unit of an ANN. One certain neuron in each layer in the network is connected to each neuron in the previous and the next layers. An ANN is a black box that can avoid difficulties in data analysis and modelling. It is suitable for data with uncertainties and a lack of structure. The BPNN is a multilayer feedforward neural network that uses an error back-propagation algorithm [29]. It is widely used in experimental data modelling, even if the mapping relationship seems complex and difficult to formulate [30].

Before establishing the BPNN model, experimental data should be normalized to improve the efficiency and sensitivity while training and to prevent overfitting. To ensure that the BPNN model has the ideal extrapolation capability, normalized pre-treatment values should be in the range of 0.2 to 0.8.

The data pre-treatment can by calculated as follows:

$$y = (0.8 - 0.2) \times \frac{x - min(x)}{max(x) - min(x)} + 0.2 \tag{13}$$

The reverse data pre-treatment can by calculated as follows:

$$x = (y - 0.2) \times \frac{max(x) - min(x)}{0.8 - 0.2} + min(x) \tag{14}$$

In Eqs. 13 and 14, x represents a certain value in the original data of each factor, and y is the corresponding value in the pre-treatment data of each factor, $max(x)$ and $min(x)$ are the maximum and minimum values in original data of each factor, respectively.

Of all of the training algorithms used in BPNN, the Levenberg-Marquardt algorithm was an optional one, as it can adjust the network training parameters automatically to ensure the network has real-time updating for its applicable training methods [31]. The common transfer functions used in BPNNs include the hyperbolic tangent sigmoid function (tansig), logarithmic sigmoid function (logsig), and linear function ($y = x$). Based on previous research [32], using the tansig function as the transfer function in the input-hidden layer and the linear function in hidden-output layer can obtain the best optimization in most BPNN modelling. For a BPNN with there or more layers, the network model can approximate a nonlinear function infinitely as long as there are sufficient neurons [33]. Therefore, the BPNN configuration used in this study contained one input layer, one hidden layer and one output layer. The neural network toolbox in MATLAB was used to establish the BPNN model.

It is important to determine the proper number of neurons in the hidden layers. Including too many neurons may lead to the problems like over-fitting and local minima. To ensure the network performance and generalization ability are sufficiently high, the structure of the network should be as compact as possible to achieve high precision. With the experimental formulas $\sum_{i=0}^{n} C_{n_1}^{i} > k$ (where k is for the number of data for the input layer, n_1 is the number of neurons in hidden layer, and n is the number of neurons in the input layer), $n_1 = \sqrt{n + m} + a$ (where m is the number of neurons in the output layer, $a \in [1,10]$) [34], and $n_1 = \log_2 n$ [35], the number of neurons was selected as 26. As a result, the BPNN with the topological structure of 3-26-4 was chosen. After training the model 49 times, the network converged.

Table 13 shows the comparison of the predicted results in this model and the practical experimental data. The total average of the error was 4.06 %. The errors in the diameter were smaller than those of roundness. The factors and scope of the parameters that affected the roundness were more complex than the diameters, which may have caused the roundness values to be more difficult to predict and have a larger deviation than the diameters. The highest error of the result was less than 7 %.

Table 13 Comparison of the predicted results in this model and the practical experimental data

Parameters		Entrance diameter, μm	Exit diameter, μm	Entrance roundness, μm	Exit roundness, μm
Test B5	Predicted result	959.89	755.54	33.03	50.96
	Actual result	983.2	777.78	30.05	49.13
	Error	2.42 %	2.86 %	9.02 %	3.59 %
Test B9	Predicted result	1051.33	993.67	37.27	30.21
	Actual result	1036.80	969.33	38.88	28.34
	Error	1.40 %	2.51 %	4.14 %	6.60 %

4. Conclusion

By laser helical drilling experiments, rules for the machining parameters and geometric morphological characteristics of micro-holes were determined in this study. In the range of 80 μJ to 130 μJ, with the single pulse energy increasing, the diameters increased. The Diameter and roundness of the entrance and exit tended to be stable, while the taper exhibited a slight change. The increase in the rotation rate of the laser can lead to a fluctuation in a range in the values of diameters, but the taper remained almost invariant. The downward focus rate had a remarkable influence on the characteristics of the micro-holes. With the defocusing rate increasing, the diameters changed greatly.

The OED shows that when the single-pulse energy was in the range of 60 μJ to 100 μJ, the focus downward rate had the most significant effect on the entrance diameter. The single-pulse energy effect has the most significant effect on the exit diameter and the roundness.

In addition, a BP neural network was used to establish a mapping relationship based on the laser parameters and characteristics of micro-holes with an average error of less than 5 % and the maximum error of less than 7 %. Thus, the results of the laser drilling experiments were predictable, and this process was convenient for optimizing the process parameters, which could be applied to industrial practice.

Further research may concentrate on exploring the effect of other laser processing parameters, and different modelling methods for constructing the mapping relationship between the laser parameters and the geometrical morphologies of the micro-holes.

Acknowledgement

The authors are grateful for the financial support provided by the National Natural Science Foundation of China (grant number 51705440), the Fundamental Research Funds for the Central Universities XMU (grant number 20720180072), the Aeronautical Science Foundation of China (grant number 20170368001), the Shenzhen Fundamental Research Program (grant number JCYJ20170818141303656), and the Natural Science Foundation of Fujian Province, China (grant number 2019J01044).

References

[1] Huang, H., Yang, L.-M., Liu, J. (2014). Micro-hole drilling and cutting using femtosecond fiber laser, *Optical Engineering*, Vol. 53, No. 5, Article No. 051513, doi: 10.1117/1.OE.53.5.051513.

[2] Rihakova, L., Chmelickova, H. (2017). Laser drilling of alumina ceramics using solid state Nd: YAG laser and QCW fiber laser: Effect of process parameters on the hole geometry, *Advances in Production Engineering & Management*, Vol. 12, No. 4, 412-420, doi: 10.14743/apem2017.4.268.

[3] Shaegh, S.A.M., Pourmand, A., Nabavinia, M., Avci, H., Tamayol, A., Mostafalu, P., Ghavifekr, H.B., Aghdam, E.N., Dokmeci, M.R., Khademhosseini, A., Zhang, Y.S. (2018). Rapid prototyping of whole-thermoplastic microfluidics with built-in microvalves using laser ablation and thermal fusion bonding, *Sensors and Actuators B: Chemical*, Vol. 255, Part 1, 100-109, doi: 10.1016/j.snb.2017.07.138.

[4] Padmanabham, G., Bathe, R. (2018). Laser materials processing for industrial applications, *Proceedings of the National Academy of Sciences, India Section A: Physical Sciences,* Vol. 88, No. 3, 359-374, doi: 10.1007/s40010-018-0523-5.

[5] Ciurana, J., Arias, G., Ozel, T. (2009). Neural network modeling and particle swarm optimization (PSO) of process parameters in pulsed laser micromachining of hardened AISI H13 steel, *Materials and Manufacturing Processes*, Vol. 24, No. 3, 358-368, doi: 10.1080/10426910802679568.

[6] Dubey, A.K., Yadava, V. (2008). Laser beam machining – A review, *International Journal of Machine Tools and Manufacture*, Vol. 48, No. 6, 609-628, doi: 10.1016/j.ijmachtools.2007.10.017.

[7] Kamlage, G., Bauer, T., Ostendorf, A., Chichkov, B.N. (2003). Deep drilling of metals by femtosecond laser pulses, *Applied Physics A*, Vol. 77, No. 2, 307-310, doi: 10.1007/s00339-003-2120-x.

[8] Zoubir, A., Shah, L., Richardson, K., Richardson, M. (2003). Practical uses of femtosecond laser micro-materials processing, *Applied Physics A*, Vol. 77, No. 2, 311-315, doi: 10.1007/s00339-003-2121-9.

[9] Gruner, A., Schille, J., Loeschner, U. (2016). Experimental study on micro hole drilling using ultrashort pulse laser radiation, *Physics Procedia*, Vol. 83, 157-166, doi: 10.1016/j.phpro.2016.08.030.

[10] Wang, X.C., Zheng, H.Y., Chu, P.L., Tan, J.L., Teh, K.M., Liu, T., Ang, B.C.Y., Tay, G.H. (2010). Femtosecond laser drilling of alumina ceramic substrates, *Applied Physics A*, Vol. 101, No. 2, 271-278, doi: 10.1007/s00339-010-5816-8.

[11] Yang, L., Kong, X., Wang, Y., Ding, Y., Zhang, H., Chi, G. (2016). Laser micro-holes machining technology and its application, *Aeronautical Manufacturing Technology*, No. 19, 271-278, doi: 10.16080/j.issn1671-833x.2016.19.032.

[12] Liu, Y., Zhang, R., Li, W., Wang, J., Yang, X., Cheng, L., Zhang, L. (2018). Effect of machining parameter on femtosecond laser drilling processing on SiC/SiC composites, *The International Journal of Advanced Manufacturing Technology*, Vol. 96, No. 5-8, 1795-1811, doi: 10.1007/s00170-017-1163-7.
[13] Dausinger, F. (2002). Femtosecond technology for precision manufacturing: Fundamental and technical aspects, In: *Proceedings of Third International Symposium on Laser Precision Microfabrication*, Osaka, Japan, doi: 10.1117/12.486506.
[14] Abeln, T., Radtke, J., Dausinger, F. (1999). High precision drilling with short-pulsed solid-state lasers, In: *Laser Institute of America – Proceedings – LIA,* Vol. 88, 195-203, doi: 10.2351/1.5059302.
[15] Liao, C., Anderson, W., Antaw, F., Trau, M. (2018). Maskless 3D ablation of precise microhole structures in plastics using femtosecond laser pulses, *ACS Applied Materials & Interfaces,* Vol. 10, No. 4, 4315-4323, doi: 10.1021/acsami.7b18029.
[16] Kraus, M., Ahmed, M.A., Michalowski, A., Voss, A., Weber, R., Graf, T. (2010). Microdrilling in steel using ultrashort pulsed laser beams with radial and azimuthal polarization, *Optics Express*, Vol. 18, No. 21, 22305-22313, doi: 10.1364/OE.18.022305.
[17] ISO 1101:2017 Geometrical product specifications (GPS) — Geometrical tolerancing — Tolerances of form, orientation, location and run-out, from *https://www.iso.org/standard/66777.html*, accessed October 27, 2019.
[18] Zhu, J., Chew, D.A.S., Lv, S., Wu, W. (2013). Optimization method for building envelope design to minimize carbon emissions of building operational energy consumption using orthogonal experimental design (OED), *Habitat International*, Vol. 37, 148-154, doi: 10.1016/j.habitatint.2011.12.006.
[19] Wang, C., Xue, S., Chen, G., Luan, D., Wang, S., Wang, Y., Wang, S., Liu, J., Wang, Z., Zhang, P. (2018). Influence of laser parameters on micro-hole drilling of Cu50Zr50 amorphous alloys foil, *Ferroelectrics*, Vol. 523, No. 1, 61-66, doi: 10.1080/00150193.2018.1391557.
[20] Fan, N.-N., Xia, Z.-D., Sun, X.-Y., Hu, Y.-W. (2016). Experimental study on stainless steel micro-hole trepanned by femtosecond laser, *Laser & Infrared,* Vol. 46, No. 10, 1200-1205, doi: 10.3969/j.issn.1001-5078.2016.10.006.
[21] Fornaroli, C., Holtkamp, J., Gillner, A. (2013). Laser-beam helical drilling of high quality micro holes, Physics Procedia, Vol. 41, 661-669, doi: 10.1016/j.phpro.2013.03.130.
[22] Wang, G.-A., Zhang, Y.-Z., Ni, X.-W., Lu, J. (2007). Effect of deviation distance to focal spot on nanosecond-pulsed-laser drilling rates in air, *Chinese Journal of Lasers*, Vol. 34, No. 12, 1621-1624.
[23] Zou, Z.-Q., Li, J., Hu, L.-Y. (2017). Diameter changing regularity with the laser parameters of nanosecond laser drilling, *Optics & Optoelectronic Technology*, Vol. 15, No. 5, 58-61.
[24] Verbeeck, J., Bertoni, G., Schattschneider, P. (2008). The Fresnel effect of a defocused biprism on the fringes in inelastic holography, *Ultramicroscopy*, Vol. 108, No. 3, 263-269, doi: 10.1016/j.ultramic.2007.06.007.
[25] Wu, X., Leung, D.Y.C. (2011). Optimization of biodiesel production from camelina oil using orthogonal experiment, *Applied Energy*, Vol. 88, No. 11, 3615-3624, doi: 10.1016/j.apenergy.2011.04.041.
[26] Li, X.J., Dong, Y.W., Yin, C.P., Zhao, Q., You, Y.C. (2018). Geometric parameters evolution experiment of hole during femtosecond laser helical drilling, *Chinese Journal of Lasers*, Vol. 45, No. 5, doi: 10.3788/CJL201845.0502008.
[27] Ren, N., Zhang, L., Wang, H., Xia, K., Shi, C. (2017). Orthogonal experiments and variance analysis in Nd:YAG pulsed laser trepanning drilling, *Laser & Optoelectronics Progress*, Vol. 54, No. 6, doi: 10.3788/LOP54.061408.
[28] Dhara, S.K., Kuar, A.S., Mitra, S. (2008). An artificial neural network approach on parametric optimization of laser micro-machining of die-steel, *The International Journal of Advanced Manufacturing Technology*, Vol. 39, No. 1-2, 39-46, doi: 10.1007/s00170-007-1199-1.
[29] Casalino, G. (2018). [INVITED] Computational intelligence for smart laser materials processing, *Optics & Laser Technology*, Vol. 100, 165-175, doi: 10.1016/j.optlastec.2017.10.011.
[30] Majumder, A. (2010). Comparison of ANN with RSM in predicting surface roughness with respect to process parameters in Nd:YAG laser drilling, *International Journal of Engineering Science and Technology*, Vol. 2, 5175-5186.
[31] Li, M., Wu, H., Wang, Y., Handroos, H., Carbone, G. (2017). Modified Levenberg–Marquardt algorithm for back-propagation neural network training in dynamic model identification of mechanical systems, *Journal of Dynamic Systems, Measurement, and Control*, Vol. 139, No. 3, Article No. 031012, doi: 10.1115/1.4035010.
[32] Guo, Q.-C., He, Z.-F. (2014). Economic forecasting model based on artificial neural network, *Computing Technology and Automation*, Vol. 33, No. 1, 132-136.
[33] Zhang, Y., Gao, X., Katayama, S. (2015). Weld appearance prediction with BP neural network improved by genetic algorithm during disk laser welding, *Journal of Manufacturing Systems*, Vol. 34, 53-59, doi: 10.1016/j.jmsy.2014.10.005.
[34] Ding, S., Su, C., Yu, J. (2011). An optimizing BP neural network algorithm based on genetic algorithm, *Artificial Intelligence Review*, Vol. 36, No. 2, 153-162, doi: 10.1007/s10462-011-9208-z.
[35] Ai, J.L., Yang, X.Z. (2017). Fault diagnosis of aero-engine based on self-adaptive neural network, *Scientia Sinica Technologica*, Vol. 48, No. 3, 326-335, doi: 10.1360/N092017-00224.